# Tunable infrared plasmonic properties of epitaxial $Ti_{1-x}Mg_xN(001)$ layers

Baiwei Wang, a Poomirat Nawarat, Kim M. Lewis, b& Panos Patsalas, Daniel Gall a\*

Optical transmission and reflection spectra in combination with ellipsometry and transport measurements on epitaxial rocksalt structure  $Ti_{1-x}Mg_xN(001)$  layers with  $0.00 \le x \le 0.49$  are employed to explore their potential as refractory infrared plasmonic material. A red-shift in the reflection edge  $\hbar\omega_e$  from 2.0 to 0.8 eV and the corresponding unscreened plasma energy  $\hbar\omega_{pu}$  from 7.6 to 4.7 eV indicate a linear reduction in the free carrier density N with increasing x. However, nitrogen vacancies in Mg rich samples act as donors, resulting in a minimum  $N = 1.6 \times 10^{22}$  cm<sup>-3</sup> for x = 0.49. Photoelectron valence-band spectra confirm the diminishing conduction band density of states and indicate a 0.9 eV decrease in the Fermi level as x increases from 0 to 0.49. The dielectric function  $\varepsilon = \varepsilon_1 + i\varepsilon_2$  can be divided into a low-energy spectral region where intraband transitions result in large negative and positive  $\varepsilon_1$  and  $\varepsilon_2$ , respectively, and a higher energy interband transition region with both  $\varepsilon_1$  and  $\varepsilon_2 > 0$ . The screened plasma energy  $E_{ps}$  that separates these two regions red-shifts from 2.6 to 1.3 eV for x = 0 - 0.39, indicating a tunable plasmonic activity that extends from the visible to the infrared (470 - 930 nm). Electron transport measurements indicate a metallic temperature coefficient of resistivity (TCR) for TiN-rich alloys with  $x \le 0.26$ , but weak carrier localization and a negative TCR < 60 K for x = 0.39 and < 300 K for x = 0.49, attributed to Mg-alloying induced disorder. The plasmonic quality factor Q is approximately an order of magnitude larger than what was previously reported for polycrystalline  $Ti_{1-x}Mg_xN$ , making  $Ti_{1-x}Mg_xN(001)$  layers competitive with  $Ti_{1-x}Sc_xN(001)$ .

**KEYWORDS**: 1. TiMgN, 2. Plasmonics, 3. Infrared, 4. Epitaxy, 5. TiN

## **INTRODUCTION**

Plasmonic resonances are collective and coherent excitations of conduction electrons caused by an incident electromagnetic wave. They affect polarization and screening within a material and amplify external fields at interfaces. Of particular interest are surface plasmon polaritons (SPP) and localized surface plasmon resonances (LSPR) which extend along planar boundaries for the former and at the surface of metallic nanoparticles for the latter, and are studied because of their diverse potential applications in micro-electronics, biosensing, photodetection, metamaterials, solar energy harvesting, telecommunications, and optical information storage.

An ideal plasmonic material exhibits a real permittivity  $\varepsilon_1$  with a steep transition from negative to positive values at the desired plasmonic response frequency and an imaginary permittivity  $\varepsilon_2$  that is small over the entire spectrum to minimize optical losses. <sup>12</sup> Gold and silver have high conductivities and low dielectric losses, and therefore fulfill most of above requirements

<sup>&</sup>lt;sup>a</sup> Department of Materials Science and Engineering, Rensselaer Polytechnic Institute, Troy, NY 12180, USA

<sup>&</sup>lt;sup>b</sup> Department of Physics, Applied Physics, and Astronomy, Rensselaer Polytechnic Institute, Troy, NY 12180, USA

<sup>&</sup>lt;sup>c</sup> Department of Physics, Aristotle University of Thessaloniki, Thessaloniki, GR-54124, Greece

and serve as the most popular plasmonic metals. However, they have a limited spectral tunability, <sup>13</sup> a relatively low melting point in nanoparticle form, <sup>14</sup> and excessive resistive losses at optical frequencies. 15 This motivates the search for alternative plasmonic materials which have a tunable resonance frequency and a high stability in nanoparticle form when exposed to elevated temperatures, a high current and/or illumination, and corrosive environments. Particularly promising are materials that can be grown ultrathin while maintaining excellent crystalline quality without de-wetting<sup>16-17</sup> and that are compatible with conventional CMOS processing and therefore facilitate device down-scaling.<sup>12, 18-19</sup> Thus, conductive transition metal nitrides (TMN) are emerging as promising plasmonic materials due to their relatively high electron mobility<sup>4, 13</sup> in combination with a high mechanical and temperature stability, <sup>20-21</sup> corrosion resistance, <sup>22-23</sup>, and CMOS-compatibility. 12, 18-19 Binary TMNs have been demonstrated to exhibit strong plasmonic responses, <sup>13, 17, 24-26</sup> and their resonance frequency can be tuned to cover the near UV, visible, and near IR ranges by forming ternary alloys. <sup>19</sup> More specifically, the introduction of group 5 (V, Nb, and Ta) and 6 (Cr, Mo, and W) elements in TiN leads to an increase in the conduction electron density and a corresponding increase in the plasmon resonance frequency towards the UV. 19, 27-28 Conversely, ternaries of TiN with an increasing content of atoms from groups 3 or 13 exhibit a decreasing electron density and a resonance shift to red and infrared, as demonstrated for Ti<sub>1-x</sub>Al<sub>x</sub>N<sup>29-30</sup> and Ti<sub>1-x</sub>Sc<sub>x</sub>N<sup>31-32</sup> alloys. However, both of these ternaries have limitations: The solubility of AlN in the B1 phase solid solution  $Ti_{1-x}Al_xN$  is limited to x < 0.7 which, in turn, limits the red shift.<sup>33</sup> On the other hand, Ti<sub>1-x</sub>Sc<sub>x</sub>N alloys have practical challenges associated with the high cost and limited purity of the Sc source metal<sup>34</sup> and a decreasing crystalline quality with increasing Sc content due to an increasing lattice constant and associated misfit with MgO substrates. 31, 35 An alternative promising option is to alloy TiN with alkaline earth elements such as Mg. This has the potential to extend the opportunities for controlling the carrier density in rocksalt structure transition metal nitrides. Simple electron counting suggests that a 50-50 Ti-toalkaline-earth ratio leads to a vanishing carrier density. 19, 36 Indeed, a tunable infrared plasmonic activity has been reported for polycrystalline Ti<sub>1-x</sub>Mg<sub>x</sub>N thin films. <sup>18-19</sup> We envision that the next step in exploring Ti<sub>1-x</sub>Mg<sub>x</sub>N as plasmonic material is to measure its optical properties from epitaxial layers, which are expected to have longer carrier lifetimes due to the absence of electron scattering at grain boundaries, yielding reduced resistive losses and therefore a higher expected SPP quality factor than for polycrystalline layers. 4, 19, 37-38

In this paper, we report on the optical properties and plasmonic performance of epitaxial  $Ti_{1-x}Mg_xN(001)$  layers  $(0.00 \le x \le 0.49)$  deposited on MgO(001) by reactive magnetron cosputering from titanium and magnesium targets in 5 mTorr pure N<sub>2</sub> at 600 °C. The incorporation of Mg in TiN causes a red-shift in the reflection edge and the corresponding unscreened plasma energy, implying a reduction of the electron density. This is confirmed by photoelectron valence-band spectra which indicate a diminishing conduction band density of states with increasing x. However, nitrogen vacancies in Mg-rich samples act as donors such that the free carrier density does not vanish when approaching x = 0.5. The real part of the dielectric function  $\varepsilon_1$  transitions from negative to positive values at the screened plasma energy, which moves to lower values with increasing x, indicating a tunable plasmonic activity that extends from the visible to the infrared range (470 - 930 nm). TiN-rich alloys exhibit metallic electron transport but alloying-induced disorder results in weak carrier localization for  $x \ge 0.39$ . The quality factor Q is an order of magnitude larger than that for previously reported polycrystalline  $Ti_{1-x}Mg_xN$  layers, indicating the envisioned improved ability to sustain surface plasmon polaritons.

#### **METHODS**

Epitaxial  $Ti_{1-x}Mg_xN(001)$  layers were deposited by reactive magnetron sputtering in 5 mTorr pure  $N_2$  onto  $10\times10\times0.5$  mm<sup>3</sup> double-side-polished MgO(001) substrates at 600 °C. The Mg to Ti ratio was controlled by the relative power applied to two magnetrons with 5-cm-diameter 99.99% pure Mg and Ti targets. More details on the substrate preparation, the deposition system, <sup>39-40</sup> the film growth procedure, the composition and the structure determination can be found in our previous publications. <sup>41-42</sup>

Optical ultraviolet-visible-near infrared (UV-Vis-NIR) transmittance T and reflectance R spectra were collected in a Perkin-Elmer Lambda 950 photospectrometer over the wavelength range  $\lambda = 300-3300$  nm in 2.5-nm-steps, using a nominally normal incident beam for T and a  $6^{\circ}$ incident angle for R measurements. The reflectance spectra were calibrated using an Al mirror reference that was cross-calibrated with the polished surface of a double-side polished MgO(001) substrate and optical constants of MgO from Palik's handbook.<sup>43</sup> The refractive index and extinction coefficient of the MgO as a function of wavelength were determined from R and T spectra and agree well (deviation < 5%) with the reported refractive index in the investigated wavelength range.<sup>43</sup> All data analyses assume normal incident light in Fresnel's equations for reflection instead of the experimental 6°, which causes a negligible (<1%) error in the presented data. Both T and R spectra are treated using a three-media model (air/film/substrate) which assumes the light passing from air to a thin film of constant thickness and parallel surfaces (top and bottom) and then to the substrate. 44-45 An iterative procedure is employed to determine the refractive index n and extinction coefficient k, which are subsequently converted into the real  $\varepsilon_1$ and imaginary  $\varepsilon_2$  parts of the dielectric function. More specifically, (i) the extinction coefficient k of a  $Ti_{1-x}Mg_xN$  layer is initially obtained from  $k = \alpha \times 4\pi/\lambda$ , where  $\alpha$  is the optical absorption coefficient that is directly determined from the measured R and T using  $\alpha = \ln([1-R]/T)/d$ .<sup>31</sup> This approximate expression accounts for reflection at the layer surface but neglects multiple reflections within the layer, Secondly, (ii) n is obtained from the measured R, keeping k constant. Thirdly, (iii)  $\alpha$  and the corresponding k are corrected using the measured T and accounting for multiple coherent reflections at the air-layer and layer-MgO interfaces as well as the incoherent reflection at the substrate back surface and the absorption in the substrate,  $^{44, 46-47}$  using n and k for the  $Ti_{1-x}Mg_xN$ layer from the previous iteration step and the measured optical constants for MgO from a bare substrate. Subsequently, steps (ii) and (iii) are repeated until n and k are converged. The convergence is quite fast (2-5 iterations), because the measured T is relatively small (< 0.2 for most spectra) and depends primarily on the absorption in the layer, while the measured R depends more strongly on n than k, since n > k for over 80% of the wavelength range. We note that this procedure yields two unique solutions for n for 4 out of the 6 layers. However, this ambiguity is removed for most wavelengths by an independent determination of n by spectroscopic ellipsometry (SE). Spectra were acquired by an ellipsometer (UVISEL by Horiba Jobin-Yvon) with a 191-2067 nm wavelength range, corresponding to photon energies of 0.6 - 6.5 eV, using a 50 meV step size and an incidence angle  $\phi = 70^{\circ}$ . <sup>48</sup> The measured ellipsometric angles  $\psi$  and  $\Delta$ are associated with the ratio  $\rho_f$  of the Fresnel reflection coefficients for s- and p-polarization  $\rho_f$  =  $r_p/r_s = \tan \psi \cdot e^{i\Delta}$ , where  $\tan \psi$  is the amplitude ratio upon reflection and  $\Delta$  is the shift of the phase  $\varphi$ . The real  $\varepsilon_1$  and imaginary part  $\varepsilon_2$  of the dielectric function  $\varepsilon = \varepsilon_1 + i\varepsilon_2$  are determined from  $\rho_f$ and the angle of incidence  $\phi$  using  $\varepsilon = \sin^2 \phi \cdot \{1 + \tan^2 \varphi \cdot [(1 - \rho_f)/(1 + \rho_f)]^2 \}$ .

X-ray photoelectron spectroscopy (XPS) valence band spectra were acquired using Al K<sub> $\alpha$ </sub> radiation (1486.6 eV) in a PHI 5000 Versaprobe<sup>TM</sup> system with a quartz crystal monochromator, a hemispherical analyzer and an 8-channel detector, operated with a 23.5 eV pass energy and a 0.2

eV step size over the binding energy range  $E_b = -2$  to 20 eV. The samples were analyzed after exposure to air but without any sputter cleaning of their surfaces, such that the XPS results are not affected by preferential sputtering which has been reported to lead to, for example, a 12% reduction in the nitrogen-to-Ti ratio during sputter cleaning of TiN with 3 keV Ar<sup>+</sup> ions. A 1.2 eV electron flood gun in conjunction with a low-energy (7 eV) ion neutralizer were employed to compensate for possible surface charging of the relatively insulating samples with high Mg content. No residual charging was detected, based on the C 1s peak position from adventitious adsorbed surface carbon that remained at 284.6  $\pm$  0.2 eV for all samples. We have chosen x-rays rather than ultraviolet radiation to acquire the valence band spectra despite the smaller energy resolution and signal-to-noise ratio, because the larger x-ray photoelectron escape depth results in a smaller sensitivity to surface contamination and defects. Provided the samples are contamination and defects.

Temperature-dependent resistivity measurements were performed using a Janis closed-cycle helium vacuum cryostat and a Keithley 2400 SourceMeter.  $1 \times 1 \text{ mm}^2$  indium contacts were pressed on the corners of each sample with wire leads to form a van der Pauw geometry. The resistances  $R_{12,43}$ ,  $R_{23,14}$ ,  $R_{34,21}$ , and  $R_{41,32}$  in both current directions were measured by switching contacts using a computer controlled Keithley 7001 Switch System that used a Keithley 7012-S  $4\times10$  Matrix Card. The sheet resistance  $R_s$  was determined from the measured resistances by iteratively solving the van der Pauw equation.<sup>51</sup> At each temperature, the system was allowed to equilibrate for 30-60 min to limit temperature fluctuations/gradients to < 0.2 K. The sheet resistance was measured from 5-300 K during both cool-down and warm-up. The two measurements are in good agreement with deviations of typically 0.5% and always < 2%, indicating good temperature reproducibility. A small measurement current of 1.0 mA was chosen such that the resistance increase due to local heating is negligible. The resistivity  $\rho = R_s \times d$  was determined from the measured  $R_s$  and the thickness d measured by x-ray reflectivity (XRR).

## RESULTS AND DISCUSSION

The data presented in this section are from a set of epitaxial  $Ti_{1-x}Mg_xN(001)$  layers with x = 0, 0.12, 0.19, 0.26, 0.39, and 0.49, as measured by XPS with an estimated uncertainty in x of  $\pm$  0.02. Their thickness d = 54.4, 49.0, 52.5, 52.0, 40.0, and 35.0 nm, respectively, as determined by XRR. All layers are fully-strained coherent epitaxial single crystals, as confirmed by x-ray diffraction  $\omega$ -2 $\theta$ scans,  $\omega$ -rocking curves,  $\varphi$ -scans, and reciprocal space maps presented in our previous reports.<sup>38</sup>, <sup>41</sup> The nitrogen-to-metal ratio is measured by Rutherford Backscattering Spectroscopy (RBS) and decreases from  $0.96 \pm 0.04$  for  $x \le 0.39$  to  $0.90 \pm 0.04$  for x = 0.49. This indicates that most layers are stoichiometric within experimental uncertainty, but that the layer with the highest Mg-content may be nitrogen deficient. We note however, that the experimental uncertainty in determining the nitrogen-to-metal ratio is relatively large, due to the low RBS scattering cross section for light elements like nitrogen. The development of nitrogen vacancies for x = 0.49 is expected, since the most stable pure magnesium nitride phase (Mg<sub>3</sub>N<sub>2</sub>) has a nitrogen-to-metal ratio of 0.67 and ligand vacancies become crucial for the structural stabilization. 45, 52-53 It is also consistent with previous first-principles simulations<sup>52</sup> and experimental data<sup>45</sup> suggesting an under-stoichiometric nitrogen concentration for Mg-rich layers. These nitrogen vacancies in Mg-rich layers act as donors and contribute to free carriers in the conduction band, which affects optical and electrical properties as discussed below.

Figure 1 shows optical spectra from epitaxial  $Ti_{1-x}Mg_xN(001)$  layers with  $0.00 \le x \le 0.49$ . The measured transmittance T is plotted vs the photon energy  $\hbar\omega = 0.6$  - 4 eV in Fig. 1(a). The transmittance for the 54.4-nm-thick TiN layer is low (< 5%) for  $\hbar\omega < 1.9$  eV and  $\hbar\omega > 4.6$  eV, and exhibits a peak of 21% at 2.9 eV. The spectra from the other samples also have a low transmittance

at low and high photon energies and a maximum that shifts to lower  $\hbar\omega = 2.7, 2.6, 2.5, 1.9, 1.7$  eV with increasing x = 0.12, 0.19, 0.26, 0.39, and 0.49. The low T at low frequencies is attributed for all layers to a high R in combination with free-carrier absorption for  $\hbar\omega$  < 1.5 eV, as shown in Figs. 1(b) and (c). This effect is strongest for TiN (x = 0), which corresponds to the layer with the highest charge carrier density. At high frequencies, T decreases with increasing  $\hbar\omega$ , which is attributed to the absorption from interband transitions, as discussed below. For example, T for the TiN layer reaches 10% at  $\hbar\omega = 3.6$  eV, which approximately matches the predicted direct interband transition energy of 3.5 eV in TiN near the  $\Gamma$  point, <sup>31</sup> associated with parallel bands leading to a high joint density of states. Fig. 1(b) shows the reflectance R spectra. The spectrum from the pure TiN layer exhibits a typical metallic reflectivity, with high reflection at low photon energies and a reflection edge where R = 0.5 at  $\hbar\omega_e = 2.0$  eV, resulting in the golden yellow color of TiN. The reflectance reaches a minimum of 17% at  $\hbar\omega_{\rm min} = 2.8(4)$  eV, which is in good agreement with previously reported optical properties of TiN, with minima of 6 - 20% at 2.7-2.9 eV. 4, 12, 18, 31, 45 The noise at  $\hbar\omega = 1.4 \text{ eV}$  is seen for all reflection spectra and is an experimental artifact caused by the switching between the UV-Vis and NIR detectors. The spectrum from the layer with x = 0.12 is qualitatively similar to that from pure TiN, however, with the reflection edge red-shifted to lower energy with  $\hbar\omega_{\rm e} = 1.8 \text{ eV}$  and  $\hbar\omega_{\rm min} = 2.8(1) \text{ eV}$ . This red-shift continues with increasing x to 0.19 and 0.26, yielding  $\hbar\omega_e = 1.7$  and 1.6 eV, respectively. The reflection edge is less pronounced for the Mgrich samples, as R < 50% over the entire measured wavelength range for x = 0.39 and 0.49. This shift in the reflection edge associated with the incorporation of Mg explains the distinct color change with increasing x that has been previously reported for  $Ti_{1-x}Mg_xN$  layers. <sup>12, 18-19, 22-23, 45, 54</sup> The inset in Fig. 1(b) summarizes the results from the reflectance measurements, showing a plot of  $\hbar\omega_{\min}$  and  $\hbar\omega_{e}$  vs Mg content x. The values for  $\hbar\omega_{\min}$  are directly obtained from the R spectra while the  $\hbar\omega_e$  values are determined from curve fitting described below. Both  $\omega_{\min}$  and  $\omega_e$  decrease monotonously with increasing x, which is attributed to the decrease in the conduction electron density and associated plasma frequency, as discussed in detail below.

Fig. 1(c) is a plot of the optical absorption coefficient  $\alpha$  as a function of  $\hbar\omega$ , as determined from the measured transmittance and reflectance spectra using an iterative procedure described in Section II. All spectra indicate absorption at low photon energies due to free carriers and at high photon energies due to inter-band transitions. The absorption at low  $\hbar\omega < 2$  eV generally decreases with increasing  $\hbar\omega$  and increasing x, as  $\omega$  approaches the plasma frequency and as the free carrier density N decreases with increasing x. We approximate the onset of valence-to-conduction interband transitions with the minimum in  $\alpha$ , which occurs for TiN at 2.9 eV, in agreement with previously reported minima of 2.6-2.9 eV. $^{31, 45, 55-56}$  The absorption minimum shifts to lower photon energies with the addition of Mg, more specifically, to 2.7, 2.5, 2.4, 1.9, and 1.8 eV for layers with x = 0.12, 0.19, 0.26, 0.39, and 0.49, respectively. These values agree with previously reported absorption minima at 2.0 and 1.7 eV for 300 nm thick  $\text{Ti}_{1-x}\text{Mg}_x\text{N}$  layers with x = 0.37 and 0.52, respectively. We attribute the decreasing optical band gap  $E_g$  to the reduction in the free carriers N, leading to a lowering of the Fermi level  $E_f$  and a corresponding reduction in the Burstein-Moss shift,  $^{57-58}$ , as discussed below.

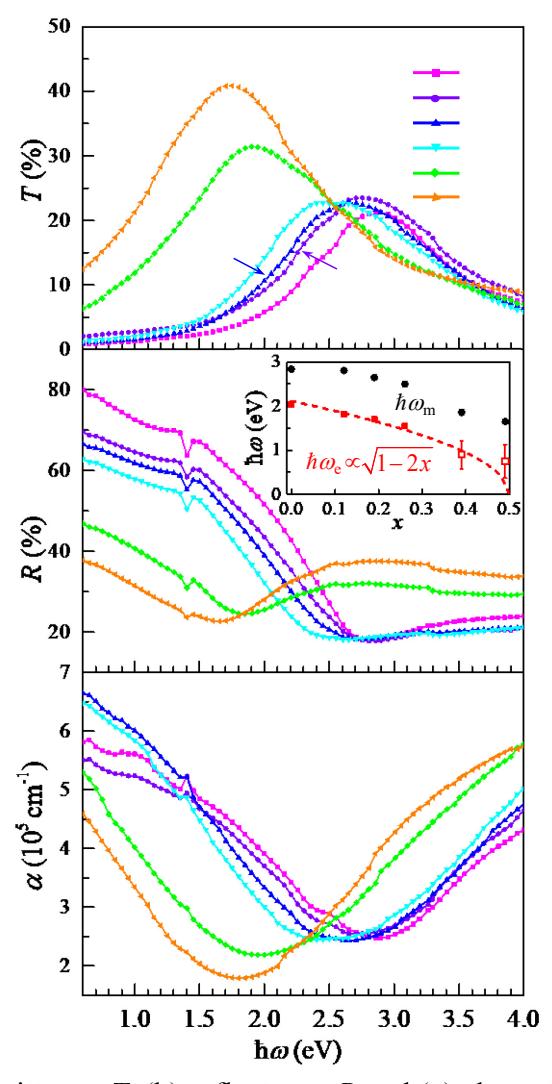


**Figure 1.** Optical (a) transmittance T, (b) reflectance R and (c) absorption coefficient  $\alpha$  vs photon energy  $\hbar\omega$  for Ti<sub>1-x</sub>Mg<sub>x</sub>N/MgO(001) layers. The inset in (b) shows the photon energy of the reflection minimum  $\hbar\omega_{min}$  and reflection edge  $\hbar\omega_{e}$  as a function of alloy composition.

Optical R and T spectra are analyzed using a Drude-Lorentz model for the complex dielectric function  $\varepsilon(\omega) = \varepsilon_1(\omega) + i\varepsilon_2(\omega)$ , 31

$$\varepsilon(\omega) = \varepsilon_{\infty} - \frac{\omega_{pu}^{2}}{\omega^{2} - i\gamma_{D}\omega} + \frac{f_{o}\omega_{o}^{2}}{\omega_{o}^{2} - \omega^{2} + i\gamma_{o}\omega}$$
(1)

where the onset of interband transitions is modeled with a Lorentz oscillator with a strength  $f_0$ , a frequency  $\omega_0$ , and damping factor  $\gamma_0$ , higher energy transitions are accounted for by the high-frequency dielectric constant  $\varepsilon_{\infty}$ , and the free carrier contribution is described with a classical Drude term where the unscreened plasma energy  $\hbar\omega_{\rm pu}$  is defined by  $\omega_{\rm pu}^2 = Ne^2/(\varepsilon_0 m^*)$ . N is the conduction electron density,  $\varepsilon_0$  the permittivity of vacuum, and  $m^*$  the electron effective mass in SI units. The free carrier damping  $\gamma_{\rm D}$  is the inverse of the carrier relaxation time. We note, the unscreened plasma energy  $E_{\rm pu} = \hbar\omega_{\rm pu}$  defined here is different from the screened plasma energy  $E_{\rm ps} = \hbar\omega_{\rm ps}$  which refers to the photon energy where  $\varepsilon_1 = 0$ , discussed below. A single oscillator cannot accurately describe the many interband transitions present in  ${\rm Ti}_{1-x}{\rm Mg}_x{\rm N}$ , but facilitates curve fitting of transmission and reflection spectra from the near infrared to (and slightly into) the

interband transition range. This is useful in the present study because the onset of interband transitions is rather close to the reflection edge, such that the Drude free electron energy range slightly overlaps with the onset of interband transitions. Simultaneous curve fitting of the measured R and T spectra from each sample provides values for the six fitting parameters in Eq. (1). A typical result for the Ti<sub>0.88</sub>Mg<sub>0.12</sub>N layer is shown in Fig. 2, where the dashed lines represent the fitted curves while the open blue squares and magenta circles are the measured R and T over a fitting range of 0.6 - 4.0 eV. The measured R is below the fitted curve for  $\hbar\omega$  < 1.4 eV, which we attribute to an experimental artifact associated with an increasing beam alignment sensitivity with decreasing  $\hbar\omega$  when operating the NIR PbS detector < 1.4 eV. The reflection edge  $\hbar\omega_e$  is determined from the fitted curve and is used for the inset in Fig. 1(b), which shows a relatively large experimental uncertainty for x = 0.39 and 0.49 as the edge approaches the lower end of the measured photon energy range. The overall good quantitative agreement between measured and fitted data, indicates that the Ti<sub>1-x</sub>Mg<sub>x</sub>N optical properties are well described by the Drude-Lorentz model.

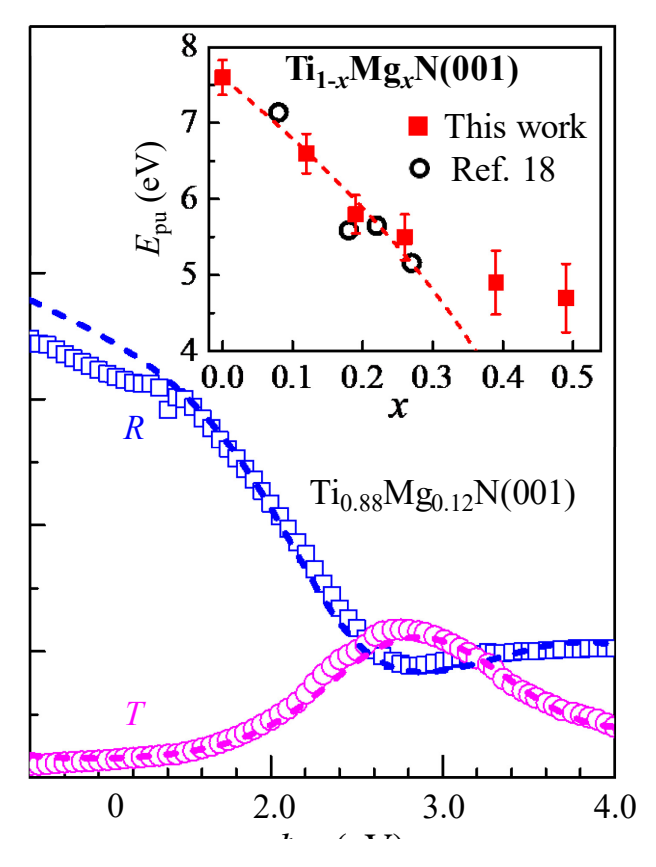


**Figure 2**. Typical transmittance T and reflectance R spectra from a Ti<sub>0.88</sub>Mg<sub>0.12</sub>N(001) layer. Dashed lines are from data fitting with the Drude-Lorentz model. The inset shows the unscreened plasma energy  $E_{pu}$  vs x in Ti<sub>1-x</sub>Mg<sub>x</sub>N.

The inset in Fig. 2 shows the unscreened plasma energy  $E_{pu} = \hbar \omega_{pu}$  as a function of x, determined from optical curve fitting and plotted as red squares. The plot includes also open black circles that denote the previously reported  $E_{pu}$  values from polycrystalline  $T_{i_1-x}Mg_xN$  layers deposited by a hybrid reactive arc evaporation-magnetron sputtering method, showing good quantitative agreement with our data. The unscreened plasma energy  $\hbar \omega_{pu}$  is related to the

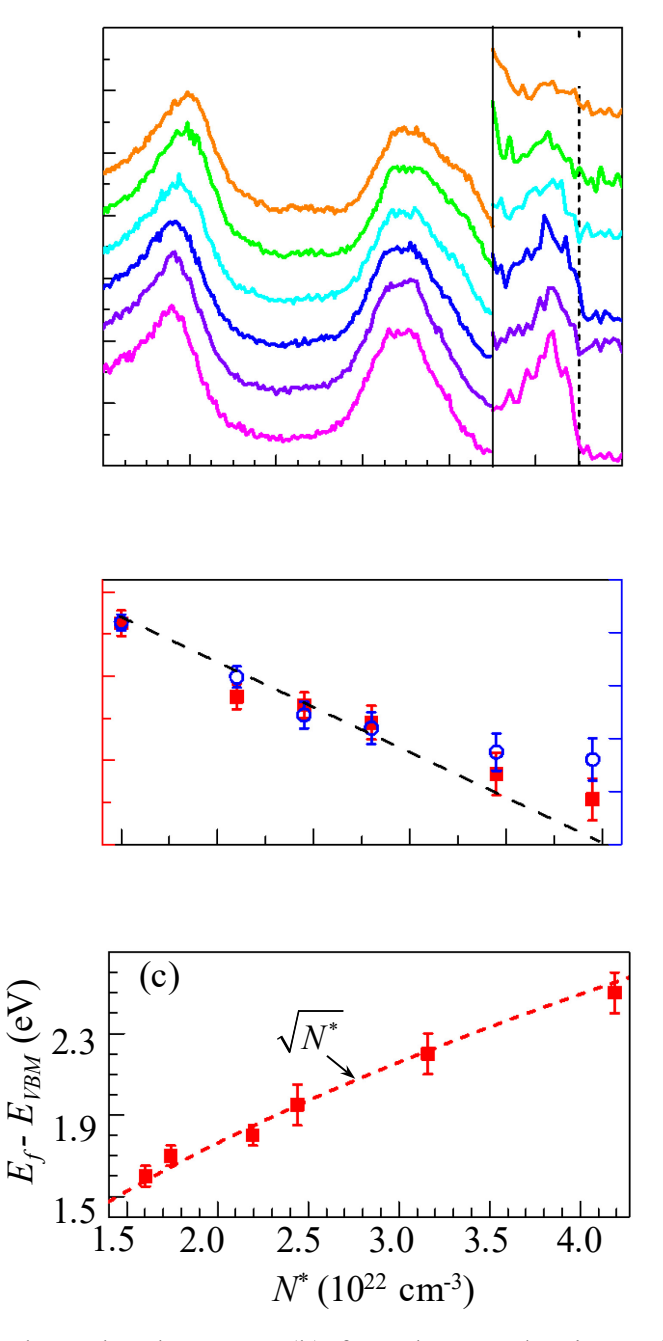
conduction electron density N through  $\omega_{pu} \propto \operatorname{sqrt}(N)$ , assuming  $m^*$  is composition independent. Furthermore, N is expected to be proportional to (1-2x), since the conduction band contains one electron per formula unit for TiN but each substitution of a Ti by a Mg atom is expected to reduce the free electron concentration by two. Correspondingly, the red dashed line in the inset is obtained from curve fitting using the first four data points and  $\hbar\omega_{pu} \propto \text{sqrt}(1-2x)$ , yielding a curve that approaches zero at x = 0.5, in agreement with the expected vanishing free carrier concentration and the reported metal-to-semiconductor transition at x = 0.5 in  $Ti_{1-x}Mg_xN$  alloys. <sup>42, 52, 59</sup> A similar trend as a function of composition x is also observed for the reflection edge  $\omega_e$  plotted in the inset of Fig. 1(b). We use  $\hbar\omega_e \propto \operatorname{sqrt}(1-2x)$  for the dashed line in Fig. 1(b) since the reflection edge is proportional to  $\omega_{pu}$  if the composition-dependence of electron scattering, interband transitions, and the screening of plasma oscillations due to valence electron polarization is negligible.<sup>31</sup> We measure  $E_{pu} = 7.6$  eV for TiN (x = 0.0), which is within the range of previously reported values of 4.5-9.8 eV,<sup>4</sup> and also within the narrower range of 6.9-8.0 eV from the majority of the studies.<sup>4,31</sup>, <sup>55</sup> Increasing the Mg content in the alloy reduces  $E_{pu}$  to 6.6, 5.8, and 5.5 eV for x = 0.12, 0.19, and 0.26, respectively. The first four data points with  $0.0 \le x \le 0.26$  are in good agreement with the dashed line. However,  $E_{pu} = 4.9$  and 4.7 eV for x = 0.39 and 0.49 are above the curve, which we attribute to free carriers induced by nitrogen vacancies. The fitting procedure provides also values for the electrical resistivity  $\rho$ , determined from the free carrier damping term  $\gamma_D$  using  $\rho = (4\pi/\hbar) \cdot \gamma_D$  $/\omega_{\rm pu}^2$ . This resistivity from our optical fitting is larger than from direct electronic transport measurements for most samples, with  $\rho = 122$  (15.9), 175 (23.6), 188 (41.4), 188 (43.8), 346 (202.7) and 354 (434.1)  $\mu\Omega$ ·cm for x = 0.0, 0.12, 0.19, 0.26, 0.39, and 0.49, respectively, where the values in the parentheses are from transport measurements. The large deviation between these two data sets for Ti-rich alloys (small x) is attributed to an overestimation of the resistivity by the optical method which uses a Drude free electron model that cannot correctly account for multiple partially filled bands with varying effective masses. More specifically, for TiN and Ti<sub>1-x</sub>Mg<sub>x</sub>N alloys with a small x, three d-bands with different curvatures cross the Fermi level near the  $\Gamma$ -point as well as near the Brillouin zone boundary close to W- and K-points, resulting in electron transport characterized by a sum of carriers with different effective masses and mobilities which are not correctly described by the optical Drude model. However, increasing x lowers the Fermi level such that the two upper bands are depleted of electrons, and charge carriers only occupy states in the lowest d conduction band. This band exhibits both negative and positive curvatures near  $\Gamma$  and W, respectively, causing a continued optical resistivity overestimation until the Fermi level approaches the band minimum at the X point (as x approaches 0.5), where the band is nearly parabolic and the Drude free electron model is fully applicable. A similar divergence has previously been reported for Ti-rich Ti<sub>1-x</sub>Sc<sub>x</sub>N alloys.<sup>31</sup>

Figure 3(a) shows XPS valence-band spectra from  $Ti_{1-x}Mg_xN(001)$  layers with x = 0-0.49. The detected photoelectron intensity is plotted vs the electron energy E, with the zero-energy set to the Fermi level  $E_f$ . The data near  $E_f$  is magnified by expanding the x-axis scale between -2 and 1 eV, and multiplying the plotted XPS intensity in that range by a factor of 5. The spectra exhibit three characteristic features that are well known for cubic transitional-metal (TM) nitrides from both computational<sup>52,59</sup> and experimental<sup>27,42</sup> studies, and are associated with nitrogen 2s semicore states, hybridized N 2p-TM d states with  $e_g$  symmetry, and non-bonding TM d states with  $t_{2g}$  symmetry that define the conduction band. The term non-bonding here refers to TM orbitals that do not hybridize with N 2p orbitals and therefore cause no bonding between metal and nitrogen atoms, although they contribute to metal-metal bonding. The TiN (t = 0.0) spectrum in Fig. 3 is in good agreement with previously reported spectra for TiN, t = 0.0 spectrum in Fig. 3 is in good agreement with previously reported spectra for TiN, t = 0.0 spectrum in Fig. 3 is in good agreement with previously reported spectra for TiN, t = 0.1 eV. The measured density of states

(DOS) has a pronounced minimum approximately 2 eV below  $E_f$ . The intensity increase between -2 eV and the Fermi level is associated with the non-bonding Ti 3d states that form the TiN conduction band which contains one electron per formula unit and results in metallic conduction. We note that the decrease between -0.5 and 0.0 eV is due to experimental broadening, since the Al  $K_{\alpha}$  x-ray source has an approximately 1 eV width and correspondingly yields only an approximately 1 eV resolution in the measured valence band spectrum. The spectrum from the  $Ti_{1-x}Mg_xN(001)$  layer with x = 0.12 is similar to that for TiN. However, the N 2s peak is shifted by 0.1 eV to -16.7 eV and the DOS between -2 to 0 eV is considerably reduced. The right shift of the N 2s peak to lower binding energy is associated with the lower Pauling electronegativity of Mg(1.32) than of Ti(1.55).<sup>60</sup> Alternatively, this shift can also be attributed to the lowering of the Fermi-level, since the 24% lower carrier-concentration of this sample in comparison to TiN reduces  $E_f$  by approximately 0.3 eV, or correspondingly, is expected to cause a 0.3 eV right-shift of the measured spectrum. The diminishing DOS below  $E_f$  is a clear indication of the decreasing free carrier density in the conduction band. A similar but opposite trend has previously been reported for Ti<sub>1-x</sub>W<sub>x</sub>N and Ti<sub>1-x</sub>Mo<sub>x</sub>N XPS valence-band spectra, where an increasing concentration of group 6 elements leads to a larger free electron density and a corresponding increase in the feature below  $E_f$ . <sup>27,50</sup> Conversely, increasing the Mg content in our Ti<sub>1-x</sub>Mg<sub>x</sub>N(001) layers to 0.19, 0.26, 0.39 and 0.49 leads to a continuous decrease in the DOS below  $E_f$ , leaving it barely detectable for x = 0.49. Simultaneously, the N 2s peak continues to shift to higher energies, reaching -16.0 eV for x = 0.49.

Figures 3(b) and (c) show the results from a quantitative analysis of the measured photoelectron spectra. For this purpose, the position of the valence band maximum EVBM is determined for each spectrum from the x-intercept of a tangent line to the right side of the hybridized N 2p-Ti/Mg 3d feature, yielding for example  $E_{VBM} = -2.5$  eV for TiN. Subsequently, the free electron density N is determined from the area under the measured curves between  $E_{\mathrm{VBM}}$ and  $E_f$ , scaled by a TiN cation density of  $5.3 \times 10^{22}$  cm<sup>-3</sup> and plotted vs the Mg content x as red squares in Fig. 3(b). This free electron density decreases from  $N = 5.3 \times 10^{22}$  cm<sup>-3</sup> for x = 0 to 3.5, 3.3, 2.9, 1.7, and  $1.1 \times 10^{22}$  cm<sup>-3</sup> for x = 0.12, 0.19, 0.26, 0.39, and 0.49, respectively. Fig. 3(b) also includes as blue circles the optical effective free electron density  $N^* = N(m_e/m^*)$ , as obtained from the unscreened plasma frequency using  $N^* = \varepsilon_0 m^* \omega_{\text{Du}}^2 / e^2$  where  $m_e$  is electron mass.<sup>31, 54</sup>  $N^*$ =  $4.2 \times 10^{22}$  cm<sup>-3</sup> for TiN (x = 0), which is close to a previously reported  $N^* = 4.6 \times 10^{22}$  cm<sup>-3</sup>. <sup>31</sup>  $N^*$ decreases continuously to 3.2, 2.4, 2.2, 1.7, and  $1.6 \times 10^{22}$  cm<sup>-3</sup> for x = 0.12, 0.19, 0.26, 0.39, and 0.49, respectively. The last value agrees with a previously reported  $N^* = 1.4 \times 10^{22}$  cm<sup>-3</sup> for  $Ti_{0.5}Mg_{0.5}N.^{54}$  Thus, both N and N\* show a similar composition dependence with a linear decrease as indicated by the dashed line in Fig. 3(b). This line reaches zero at x = 0.5 which corresponds to the 50-50 Ti-to-Mg ratio for which the density of free carriers is expected to vanish. We note, the data points for x = 0.39 and 0.49 are considerably above the dashed line, which is attributed to additional free carriers due to nitrogen vacancies, as discussed above. Correspondingly, we expect a considerable Burstein-Moss shift even for the Ti<sub>0.51</sub>Mg<sub>0.49</sub>N layer and interpret the aforementioned minimum in  $\alpha$  at 1.8 eV in Fig. 1(c) as an upper bound for the Ti<sub>0.5</sub>Mg<sub>0.5</sub>N band gap. Considering the approximately linear increase in the conduction band DOS, 52 we estimate a maximum Burstein-Moss shift of 1 eV and conclude that our results suggest a band gap for  $Ti_{0.5}Mg_{0.5}N$  of 0.8-1.8 eV, consistent with the predicted bandgap  $E_g = 1.1$ -1.3 eV for  $Ti_{0.5}Mg_{0.5}N$ by first-principles calculations<sup>52</sup> and the experimentally determined value of 0.7-1.7 eV. <sup>42, 45, 52</sup> Fig. 3(c) shows the Fermi level vs the free electron density. More specifically, the energy difference  $\Delta E = E_f - E_{VBM}$  is plotted vs  $N^*$ , indicating a continuous increase in  $E_f$  with an increasing electron density in the Ti 3d conduction band. The dashed line in the figure is obtained from data fitting.

For this purpose, the conduction band DOS is assumed to increase linearly with energy, consistent with the reported DOS from first-principles calculations.<sup>52</sup> Correspondingly,  $\Delta E$  is expected to be proportional to the square root of  $N^*$ , and fitting yields  $\Delta E = 1.25 \times \sqrt{N^*}$ , where  $\Delta E$  and  $N^*$  are in units of eV and  $10^{20}$  cm<sup>-3</sup>, respectively. The data points follow the trend line well, indicating that the free electron density is directly tuned by Fermi level in Ti<sub>1-x</sub>Mg<sub>x</sub>N alloys.



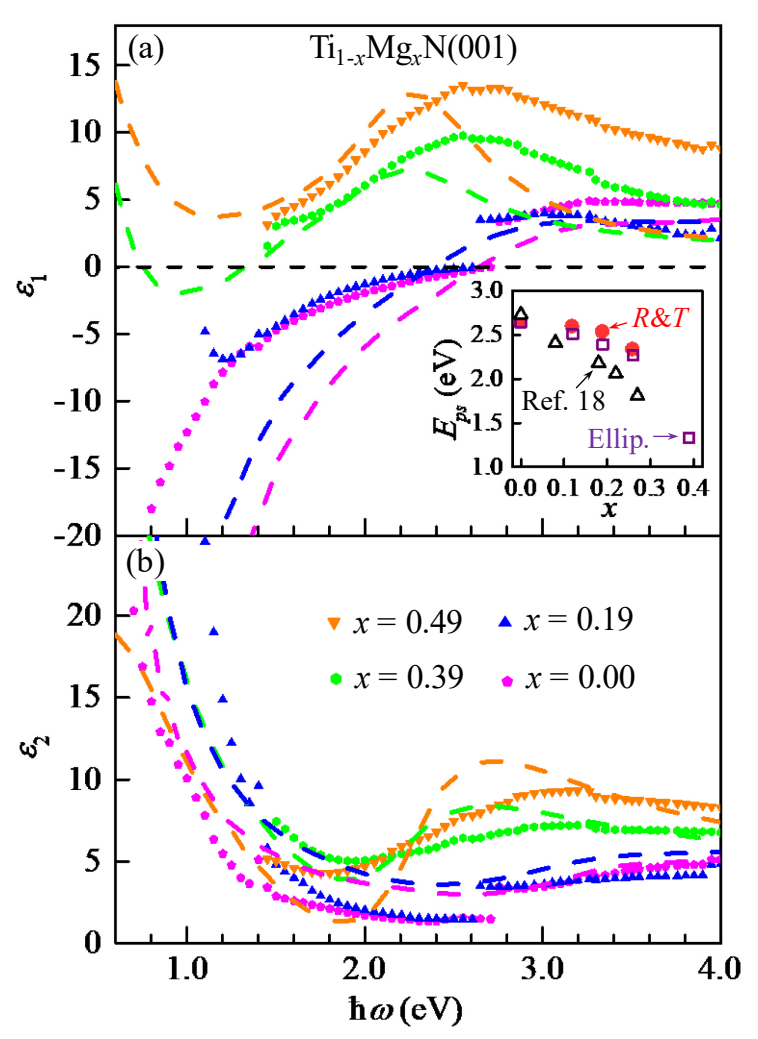
**Figure 3**. (a) XPS valence-band spectra, (b) free electron density N (red squares) and optical effective carrier density  $N^*$  (blue circles) vs Mg content x, and (c) energy difference between the Fermi level  $E_f$  and valence band maximum  $E_{VBM}$  vs  $N^*$  from  $Ti_{1-x}Mg_xN(001)$  layers.

Figure 4 is a plot of the real  $\varepsilon_1$  and imaginary  $\varepsilon_2$  parts of dielectric function vs photon energy  $\hbar\omega = 0.6 - 4.0$  eV from  $Ti_{1-x}Mg_xN(001)$  layers with x = 0.0, 0.19, 0.39 and 0.49. The spectra from the x = 0.12 and 0.26 layers are similar to the plotted x = 0.19 spectrum and are not shown for clarity purposes. The  $\varepsilon$  values are independently determined from reflectance and transmittance (R & T) spectra and from ellipsometry measurements, and are shown as data points and dashed lines, respectively. There is qualitative agreement between the two data sets with, however, some quantitative deviations, providing an estimate of the experimental uncertainty of the optical analysis from these two independent measurements. We expect that the data from R&T measurements to be particularly reliable in the high-absorption regime where the measured transmission is dominated by the absorption in the bulk and is relatively insensitive to surface effects including roughness and adsorbed impurities and oxidation. In contrast, ellipsometry becomes more reliable in regions of low  $\varepsilon_2$ , as ellipsometry does not require an absolute calibration of the reflected intensity. The values used in the following discussion are, if not specified differently, from the analysis from R&T measurements. We note that, as mentioned in the experimental procedure, the R&T analysis yields two unique solutions for n for four out of the six layers. This ambiguity is reduced by an independent determination of *n* by ellipsometry and results in a discontinuity near  $\hbar\omega = 2.7$  eV. The  $\varepsilon_1$  spectrum for TiN (x = 0.0) exhibits a typical metallic shape, with large negative values at low photon energies and a steep but featureless increase to reach  $\varepsilon_1 = 0$  at  $\hbar \omega = 2.64$  eV and a plateau of  $\varepsilon_1 = 4.5 \pm 0.3$  for  $\hbar \omega > 3.2$  eV. This is in good quantitative agreement with previous reports and is attributed to intra- and inter-band transitions at low and high photon energies, respectively. <sup>4,31,55-56,61</sup> The  $\varepsilon_1$  spectra for the x = 0.12, 0.19, and 0.26 layers are qualitatively similar to that for TiN, and indicate a gradual redshift of the photon energy where  $\varepsilon_1$  becomes positive, with  $\hbar\omega(\varepsilon_1=0)=2.59,\,2.53,\,$  and 2.33 eV, respectively. In contrast, increasing x further to 0.39 and 0.49 leads to qualitatively different spectra. They exhibit local maxima of  $\varepsilon_1 = 9.8$  and 13.5 at  $\hbar\omega = 2.6$  eV which are attributed to the onset of direct interband transitions at the X-point, similar to the reported  $\varepsilon_1$  peaks at 2.9 eV in polycrystalline  $Ti_{0.73}Mg_{0.27}N^{19}$  and at 2.09 eV in ScN. <sup>34</sup> The plotted  $\varepsilon_1$  for these two samples remains positive over the entire measured R & T photon energy range, similar to the positive  $\varepsilon_1$  spectra that have been reported for semiconducting nitrides such as ScN<sup>62</sup> and for Ti<sub>1-x</sub>RE<sub>x</sub>N and Ti<sub>-x</sub>AE<sub>x</sub>N layers, where RE = Sc, Y, and La and AE = Mg and Ca. 19 Our ellipsometry measurements include lower photon energies and can detect an  $\hbar\omega(\varepsilon_1 = 0) = 1.33$  eV for x = 0.39, but no crossover point where  $\varepsilon_1 = 0$ for x = 0.49, consistent with the expected metal-insulator transition with increasing x. We note that the ellipsometry analyses indicate positive  $\varepsilon_1$  for  $\hbar\omega < 1.0$  eV for both x = 0.39 and 0.49, suggesting a transition to semiconducting properties at large x. This is qualitatively consistent with the carrier localization detected by our transport measurements, but deviates quantitatively from the degenerate (metallic) conduction measured for x = 0.39 as presented below. This deviation may be attributed to the surface sensitivity of the ellipsometry measurements which is affected by surface oxidation of the  $Ti_{1-x}Mg_xN(001)$  layers.

We refer to the photon energy where  $\varepsilon_1 = 0$  as the screened plasma energy  $E_{ps} = \hbar \omega_{ps}$ .  $E_{ps}$  separates the  $\varepsilon$  spectra into a low energy region where  $\varepsilon_1 < 0 < \varepsilon_2$  such that light is reflected by conduction electrons and the skin depth is infinitely small,  $^{12}$  and a high energy region where  $\varepsilon_1 > 0$  and  $\varepsilon_2 > 0$ , leading to a semitransparent nitride with moderate light attenuation caused by interband absorption.  $E_{ps}$  is particularly important for plasmonic devices since it has been found to be proportional to the SPP and LSPR frequencies for binary and ternary nitride nanostructures.  $^{4}$ ,  $^{12-13}$ ,  $^{18-19}$  Correspondingly, we plot as inset in Fig. 4(a) the measured  $E_{ps}$  vs Mg content x in  $Ti_{1-x}Mg_xN(001)$ , as determined from transmission and reflection spectra (red circles) and from

ellipsometry (purple squares). There is good agreement between  $E_{ps}$  from these two independent measurements, with a maximum 6% deviation.  $E_{ps}$  for x=0.39 is only determined from the ellipsometry since it is below the measured R & T frequency range, as discussed above. The measured  $E_{ps}=2.64$  eV for TiN is in excellent agreement with the reported 2.65 eV for stoichiometric TiN layers<sup>4, 12</sup> and results in the observed bright golden color.  $E_{ps}$  decreases with increasing x to 1.33 eV for x=0.39, indicating that the plasmonic resonance can be tuned from the visible ( $\lambda_{ps}=470$  nm) to the deep infrared ( $\lambda_{ps}=930$  nm) spectral range. The monotonic decrease in  $E_{ps}$  is directly attributed to the decreasing conduction electron density as Ti atoms are substituted by Mg atoms, similar to what has previously been reported for ternary nitrides Ti<sub>1-x</sub>A<sub>x</sub>N where A = Sc, Y, and Ca.<sup>12, 18, 63</sup> The inset also includes the  $E_{ps}$  values from a previous study on polycrystalline Ti<sub>1-x</sub>Mg<sub>x</sub>N layers.<sup>18</sup> They are plotted as open triangles and indicate reasonable quantitative agreement with slightly lower energies for the polycrystalline layers which may be attributed to carrier trapping by grain boundary defect states.

Figure 4(b) shows the imaginary parts  $\varepsilon_2(\omega)$  of the dielectric functions, providing additional insight into the electronic structure, particularly the joint DOS.<sup>24, 63</sup>  $\varepsilon_2$  of TiN (x = 0.0) decreases rapidly from 29.8 to 10.1 to 1.7 for  $\hbar\omega = 0.6$ , 1.0 and 2.0 eV, respectively, before rising slightly to 4.5 at  $\hbar\omega = 3.5$  eV. Data fitting in the infrared ( $\hbar\omega \le 2.0$  eV) region indicates  $\varepsilon_2 \propto$  $(\hbar\omega)^{-2.4}$ . Thus, the decrease is less steep than the expected  $\varepsilon_2 \propto (\hbar\omega)^{-3}$  from the Drude model, <sup>64</sup> suggesting that, in addition to the dominant intraband contribution, there is an & contribution from interband transitions even for  $\hbar\omega \le 2$  eV. This is consistent with the reflection spectrum shown in Fig. 1(b) where the onset of interband transitions is close to the reflection edge and data fitting suggests a slight overlap of energy ranges for the Drude free electrons and interband transitions. At  $\hbar\omega > 2.0$  eV,  $\varepsilon_2$  increases due to interband transitions from N(:Ti)-2p states that have been reported to be 2.5–5.5 eV below the Fermi level, 4 to Ti-3 $d(t_{2g})$  states that form the conduction band, consistent with the selection rules for photonic excitation ( $\Delta l = 0, \pm 1$ ). The increase in  $\varepsilon_2$  at  $\hbar \omega >$ 3 eV is in good agreement with previously reported work<sup>4,31,56,61</sup> and is consistent with the XPS valence band spectrum where the onset of the N-2p feature is at 3.0  $\pm$  0.5 eV below E<sub>f</sub>. First principles density-of-states calculations support this interpretation as they predict a local maximum in the N-2p band at 3.5 eV below the Fermi level. The \varepsilon\_2 spectrum from the Ti<sub>0.74</sub>Mg<sub>0.26</sub>N layer is nearly identical to the TiN spectrum. In contrast, a further increase in the Mg content to x = 0.39and 0.49 results in an emerging  $\varepsilon_2$  peak at  $\hbar\omega = 2.6 \pm 0.1$  eV which is attributed to an absorption band associated with a transition from N(:Mg)-2p to Ti-3d.<sup>19</sup> This is consistent with results from reported first-principles calculations indicating that the N(:Ti)-2p and Ti-3d hybrid states are 2.5 -8.0 eV below the Fermi energy for TiN, but that the corresponding bands for hypothetical B1-MgN are only 0.0 - 5.0 eV below  $E_f$ . In addition, the nitrogen vacancies in Mg-rich samples are expected to break the translational symmetry and therefore relax the momentum conservation for intraband transitions, 64 resulting in a higher contribution from interband transitions to  $\varepsilon_2$ , and therefore a higher measured  $\varepsilon_2$  for  $x \ge 0.39$  than for  $x \le 0.19$ , for  $\hbar \omega > 2.0$  eV.



**Figure 4**. (a) Real part  $\varepsilon_1$  and (b) imaginary part  $\varepsilon_2$  of the dielectric function vs photon energy  $\hbar\omega$  for  $\mathrm{Ti}_{1-x}\mathrm{Mg}_x\mathrm{N}/\mathrm{MgO}(001)$  layers, determined from reflectance and transmittance spectra (data points) and ellipsometry (dashed lines). The inset in (a) shows the screened plasma energy  $E_{\mathrm{ps}}$  of  $\mathrm{Ti}_{1-x}\mathrm{Mg}_x\mathrm{N}$  layers as a function of alloy composition x.

Figure 5 shows the electrical resistivity  $\rho$  as a function of temperature T between 5 and 300 K for Ti<sub>1-x</sub>Mg<sub>x</sub>N(001) layers. The TiN (x=0.0) resistivity is 5.8  $\mu\Omega$ ·cm at 5 K, remains approximately constant up to 50 K, increases linearly with  $d\rho/dT=4.5\times10^{-8}~\Omega$ ·cm·K<sup>-1</sup> for  $T>100~\rm K$  due to electron-phonon scattering, and reaches  $\rho_{300\rm K}=15.9~\mu\Omega$ ·cm at room temperature. This value is slightly larger than  $\rho_{300\rm K}=12.5$ -13.0  $\mu\Omega$ ·cm reported for the highest quality epitaxial TiN(001) layers grown at  $T_s=750$ -950 °C,  $^{31,65-66}$  but is consistent with the reported increase in  $\rho$  to 17.3  $\mu\Omega$ ·cm with decreasing  $T_s=750$ -950 °C that is attributed to an increasing point defect concentration which also more dramatically affects the low-temperature TiN resistivity with a reported decreasing  $\rho=4.0, 2.1, 0.73$ , and  $0.45~\mu\Omega$ ·cm with increasing  $T_s=650, 750, 850, 950$  °C.  $^{31,65}$  The  $\rho(T)$  plots in Fig. 5(a) from TiN-rich Ti<sub>1-x</sub>Mg<sub>x</sub>N alloys with x=0.12, 0.19, and 0.26 exhibit a similar metallic temperature dependence, with a low-temperature  $\rho=11.7, 26.8$ , and 30.5  $\mu\Omega$ ·cm, a  $d\rho/dT=5.1, 6.5$ , and  $6.0\times10^{-8}~\Omega$ ·cm·K<sup>-1</sup>, and a room temperature resistivity  $\rho_{300\rm K}=23.6, 41.4$ , and 43.8  $\mu\Omega$ ·cm. A further increase in the Mg content leads to a considerably larger resistivity, with  $\rho_{5\rm K}=196~\mu\Omega$ ·cm and  $\rho_{300\rm K}=203~\mu\Omega$ ·cm for Ti<sub>0.61</sub>Mg<sub>0.39</sub>N as shown in Fig. 5(b).

The data indicates a resistivity minimum at 60 K which is attributed to weak localization caused by the random occupation of cation sites and/or the random distribution of nitrogen vacancies, similar to what has been reported for other transition metal nitrides including CrN(001),<sup>67</sup>  $TaN_x(001)$ , <sup>68</sup>  $HfN_x(001)$ , <sup>69</sup>  $Cr_{1-x}Al_xN(001)$ , <sup>47</sup>  $Sc_{1-x}Ti_xN(001)^{31}$  and  $Ti_{1-x}W_xN(001)$ . <sup>27</sup> The finite low-temperature resistivity indicates that the Fermi level for Ti<sub>0.61</sub>Mg<sub>0.39</sub>N is above the conduction edge and, as expected from simple electron counting, is well within the conduction d band such that electron transport is best described by a weak Anderson localization. This is consistent with the finite DOS at  $E_f$  measured by photoelectron spectroscopy in Fig. 3(a), the corresponding N plotted in Fig. 3(b), and the previously reported predicted DOS of  $Ti_{1-x}Mg_xN$ .<sup>52</sup> The  $\rho$  vs T curve for the layer with x = 0.49 in Fig. 5(c) exhibits a negative slope over most of the measured temperature range, with  $\rho_{5K} = 459 \ \mu\Omega$ ·cm and  $\rho_{300K} = 434 \ \mu\Omega$ ·cm. That is, this sample continues the trend of an increasing  $\rho$  and decreasing TCR with increasing x. The insets in Figs. 5(b) and (c) are plots of the conductivity  $\sigma = 1/\rho$  vs  $T^{1/2}$ . The data points are well described by the dashed straight lines for T = 5 - 40 K for x = 0.39 and T = 10-140 K for x = 0.49, suggesting that the lowtemperature electron transport is well described by variable-range hopping caused by carrier localization, <sup>67</sup> which is evident for samples with large x because of the correspondingly small electron density at E<sub>f</sub>. Thus, we describe Ti<sub>0.51</sub>Mg<sub>0.49</sub>N as a highly degenerate semiconductor and note that the negative TCR would be much more pronounced if it would be attributed to thermal carrier activation into the conduction band of approximately 1 eV, based on the predicted 1.1-1.3  $eV^{52}$  or experimental 0.7-1.7  $eV^{42,45,52}$  gap for Ti<sub>0.5</sub>Mg<sub>0.5</sub>N.

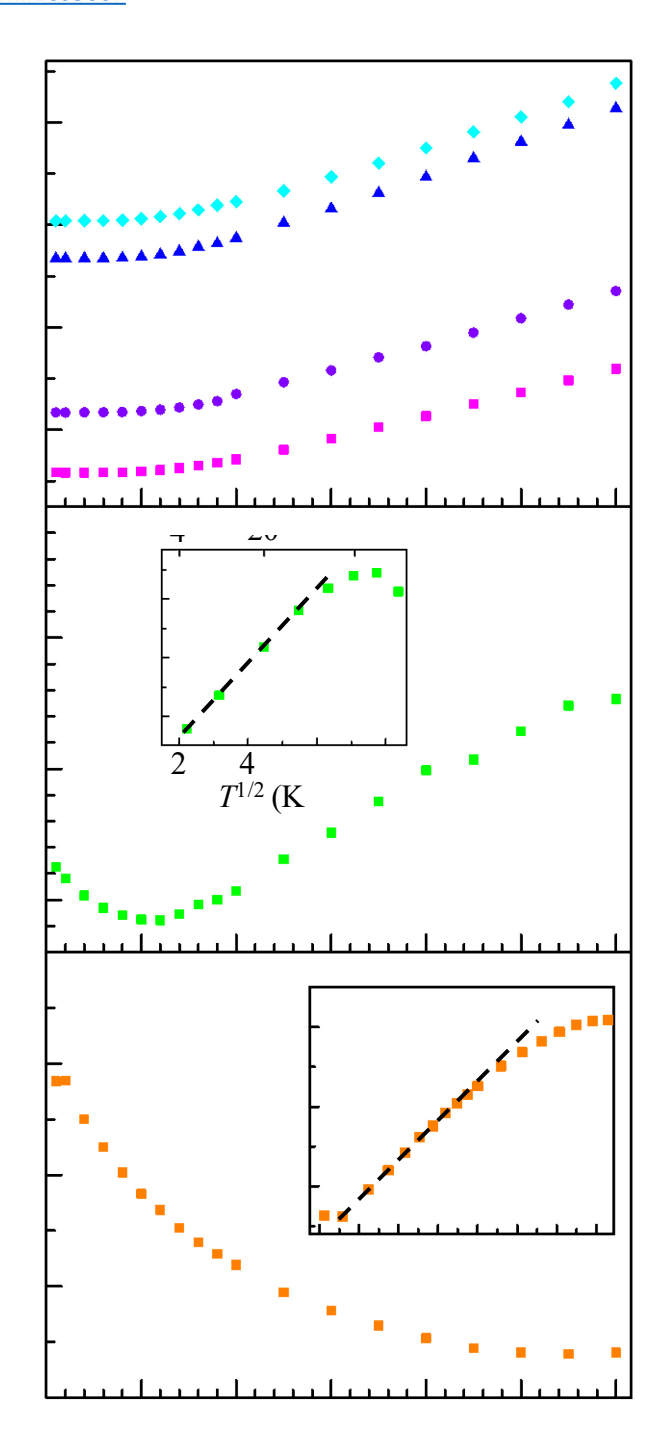


**Figure 5**. The electrical resistivity  $\rho$  vs temperature T for  $Ti_{1-x}Mg_xN(001)$  layers with (a) x = 0.00, 0.12, 0.19 and 0.26, (b) x = 0.39, and (c) x = 0.49. The insets in (b) and (c) show the conductivity  $\sigma$  vs  $T^{1/2}$ .

As a last discussion point, we estimate the plasmonic potential for  $Ti_{1-x}Mg_xN(001)$  alloys by determining the quality factor Q, which is defined as the ratio of the enhanced near field at the metal surface over the electric field of the incident light.<sup>70</sup> Q is a function of the real and imaginary permittivities  $\varepsilon_1$  and  $\varepsilon_2$  and of the nanoparticle and/or interface shape and structure.<sup>70</sup> More

specifically, O for both the LSPR of elongated spheroid nanoparticles and the SPP at an interface of a conductor with a dielectric (for  $-\varepsilon_{1,\text{metal}} >> \varepsilon_{1,\text{dielectric}}$ ) is given by the expression  $Q = \varepsilon_1^2/\varepsilon_2$ which is valid for the spectral range where  $\varepsilon_1$  is negative. <sup>70</sup> Figure 6 is a plot of  $\varepsilon_1^2/\varepsilon_2$  vs photon energy for epitaxial  $Ti_{1-x}Mg_xN(001)$  layers, as determined from the  $\varepsilon_1$  and  $\varepsilon_2$  values measured by ellipsometry and presented in Fig. 4. The dashed lines in Fig. 6 are data from polycrystalline  $Ti_{1-x}Mg_xN$  layers from Ref. 18, which are plotted for direct comparison to illustrate the benefits of epitaxial nitride growth. The solid pink line for epitaxial TiN (x = 0) shows Q values which are about half of those for Au. The curves for x = 0.12, 0.19 and 0.26 indicate that the addition of Mg to form  $Ti_{1-x}Mg_xN$  layers with increasing x = 0 - 0.26 causes a systematic redshift of the upper edge of Q, which corresponds to the crossover wavelength of  $\varepsilon_1$ . However, this shift is accompanied by a decrease in the overall Q values. This suggests that the incorporation of Mg redshifts the operation range for LSPR and SPP but reduces their effectiveness. The green solid line for epitaxial Ti<sub>0.61</sub>Mg<sub>0.39</sub>N(001) is very narrow due to the small wavelength range for which  $\varepsilon_1$  is negative. We note that the plot does not contain a green dashed line because Ref. 18 does not report dielectric functions for large x due to phase separation. The most striking result comes from the comparison of O from our epitaxial layers with the dashed lines from polycrystalline Ti<sub>1-x</sub>Mg<sub>x</sub>N from Ref. 18. The values from the epitaxial layers are approximately an order of magnitude larger. This is attributed to the reduced electron scattering at crystalline defects and at grain boundaries and illustrates the advantage of epitaxial  $Ti_{1-x}Mg_xN$ . We note that this advantage makes  $Ti_{1-x}Mg_xN$  competitive with  $Ti_{1-x}Sc_xN$ , which has previously been considered the ternary transition metal nitride with the most promising infrared plasmonic properties, <sup>18</sup> but has limited use due to the low abundance, low purity, and high cost of the Sc source material. 12, 18, 34

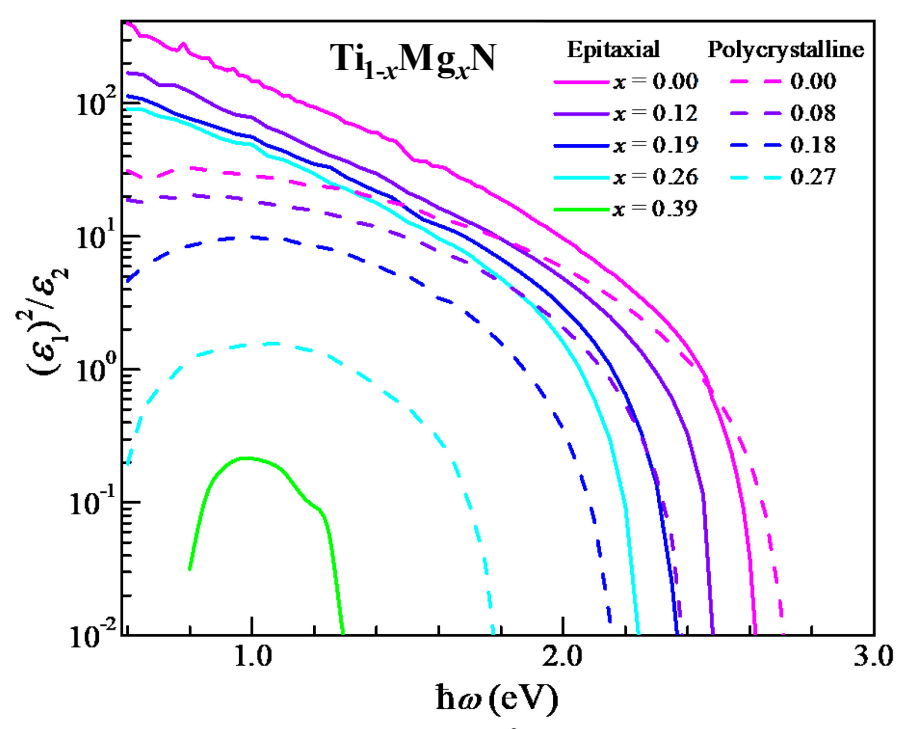


**Figure 6**. The plasmonic quality factor  $Q = \varepsilon_1^2/\varepsilon_2$  vs photon energy  $\hbar\omega$  from epitaxial  $\mathrm{Ti}_{1-x}\mathrm{Mg}_x\mathrm{N}(001)$  layers (solid lines). The dashed lines are for polycrystalline  $\mathrm{Ti}_{1-x}\mathrm{Mg}_x\mathrm{N}$  from Ref. 18.

# **CONCLUSIONS**

Single crystal Ti<sub>1-x</sub>Mg<sub>x</sub>N(001) layer are epitaxially grown on MgO(001) by reactive magnetron sputtering and their optical and plasmonic performance is investigated. Optical measurements show an increasing transparency in the intraband absorption range and a red-shift of the reflection edge  $\hbar\omega_e$  with increasing x, indicating  $\hbar\omega_e \propto (1-2x)^{1/2}$ . This confirms an effective decrease in the conduction electron density as Mg substitutes for Ti. Drude-Lorentz fitting of transmission and reflection spectra show that the unscreened plasma energy  $\hbar\omega_{\rm pu}$  decreases from 7.6 eV for TiN (x = 0.0) to 4.7 eV for x = 0.49, indicating a four-fold reduction in the free carrier density  $N \propto \omega_{\rm pu}^2$ . This is consistent with XPS valence-band spectra which show a decreasing density of filled conduction band states and a 0.9 eV decrease in the Fermi level as x increases from 0 to 0.49. Mg rich layers are under-stochiometric, with nitrogen vacancies acting as donors, resulting in a minimum  $N = 1.6 \times 10^{22}$  cm<sup>-3</sup> for x = 0.49.

The dielectric function is characterized by a negative real part  $\varepsilon_1$  and positive imaginary part  $\varepsilon_2$  for  $\hbar\omega < 2.5$  eV, and positive values of both  $\varepsilon_1$  and  $\varepsilon_2$  at higher  $\hbar\omega$ . The screened plasma energy  $E_{\rm ps}$  is tunable from visible to infrared, from 2.64 - 1.33 eV for x=0 - 0.39, corresponding to a wavelength range of 470 - 930 nm. This is attributed to the decreasing carrier density in combination with a gradual redshift of interband transitions with increasing x, due to the increasing energy of N2p states with respect to the Fermi level. Electron transport measurements indicate a metallic temperature dependence of the resistivity for TiN rich alloys with  $x \le 0.26$ , but a weak carrier localization for x=0.39 and 0.49 which is attributed to Mg-alloying induced disorder. The plasmonic quality factor Q of the epitaxial Ti<sub>1-x</sub>Mg<sub>x</sub>N(001) layers are an order of magnitude larger than the previously reported values for polycrystalline Ti<sub>1-x</sub>Mg<sub>x</sub>N, making epitaxial Ti<sub>1-x</sub>Mg<sub>x</sub>N(001) competitive with Ti<sub>1-x</sub>Sc<sub>x</sub>N.

# **AUTHOR INFORMATION**

#### **Corresponding Author**

\*Daniel Gall. Department of Materials Science and Engineering, Rensselaer Polytechnic Institute, Troy, NY 12180, USA. Email: <a href="mailto:galld@rpi.edu">galld@rpi.edu</a>

# **Current Affiliation**

&Kim M. Lewis, Department of Physics and Astronomy, Howard University, Washington, DC 20059, USA

#### **Author Contributions**

The manuscript was written through contributions of all authors. All authors have given approval to the final version of the manuscript.

#### **ACKNOWLEDGEMENTS**

The authors acknowledge financial support by the National Science Foundation under Grant Nos. 1712752, 1629230 and 1150866 (K.M.L.); and support from the Royal Thai Government Scholarship (P.N.).

#### **REFERENCES**

- 1. Garbrecht, M.; Hultman, L.; Fawey, M. H.; Sands, T. D.; Saha, B., Tailoring of surface plasmon resonances in TiN/(Al0.72Sc0.28)N multilayers by dielectric layer thickness variation. *Journal of Materials Science* **2018**, *53* (6), 4001-4009.
- 2. Murray, W. A.; Barnes, W. L., Plasmonic Materials. *Advanced Materials* **2007**, *19* (22), 3771-3782.
- 3. Catellani, A.; Calzolari, A., Plasmonic properties of refractory titanium nitride. *Phys. Rev. B* **2017**, 95 (11), 115145.
- 4. Patsalas, P.; Kalfagiannis, N.; Kassavetis, S., Optical Properties and Plasmonic Performance of Titanium Nitride. *Materials* **2015**, *8* (6), 3128.
- 5. Kassavetis, S.; Ozsdolay, B. D.; Kalfagiannis, N.; Habib, A.; Tortai, J.-H.; Kerdsongpanya, S.; Sundararaman, R.; Stchakovsky, M.; Bellas, D. V.; Gall, D.; Patsalas, P., Near-Zero Negative Real Permittivity in Far Ultraviolet: Extending Plasmonics and Photonics with B1-MoNx. *J. Phys. Chem. C* **2019**, *123* (34), 21120-21129.
- 6. Anker, J. N.; Hall, W. P.; Lyandres, O.; Shah, N. C.; Zhao, J.; Van Duyne, R. P., Biosensing with plasmonic nanosensors. *Nature Materials* **2008**, *7* (6), 442-453.
- 7. Konstantatos, G.; Sargent, E. H., Nanostructured materials for photon detection. *Nature Nanotechnology* **2010**, *5* (6), 391-400.
- 8. Naik, G. V.; Saha, B.; Liu, J.; Saber, S. M.; Stach, E. A.; Irudayaraj, J. M. K.; Sands, T. D.; Shalaev, V. M.; Boltasseva, A., Epitaxial superlattices with titanium nitride as a plasmonic component for optical hyperbolic metamaterials. *Proceedings of the National Academy of Sciences* **2014**, *111* (21), 7546-7551.
- 9. Boriskina, S. V.; Ghasemi, H.; Chen, G., Plasmonic materials for energy: From physics to applications. *Materials Today* **2013**, *16* (10), 375-386.
- 10. Li, X.; Jiang, T.; Shen, L.; Deng, X., Subwavelength guiding of channel plasmon polaritons by textured metallic grooves at telecom wavelengths. *Appl. Phys. Lett.* **2013**, *102* (3), 031606.
- 11. Siozios, A.; Koutsogeorgis, D. C.; Lidorikis, E.; Dimitrakopulos, G. P.; Kehagias, T.; Zoubos, H.; Komninou, P.; Cranton, W. M.; Kosmidis, C.; Patsalas, P., Optical Encoding by Plasmon-Based Patterning: Hard and Inorganic Materials Become Photosensitive. *Nano Letters* **2012**, *12* (1), 259-263.
- 12. Patsalas, P.; Kalfagiannis, N.; Kassavetis, S.; Abadias, G.; Bellas, D. V.; Lekka, C.; Lidorikis, E., Conductive nitrides: Growth principles, optical and electronic properties, and their perspectives in photonics and plasmonics. *Materials Science and Engineering: R: Reports* **2018**, *123*, 1-55.
- 13. Patsalas, P., Zirconium nitride: A viable candidate for photonics and plasmonics? *Thin Solid Films* **2019**, *688*, 137438.
- 14. Alarifi, H. A.; Atiş, M.; Özdoğan, C.; Hu, A.; Yavuz, M.; Zhou, Y., Determination of Complete Melting and Surface Premelting Points of Silver Nanoparticles by Molecular Dynamics Simulation. *J. Phys. Chem. C* **2013**, *117* (23), 12289-12298.
- 15. Boltasseva, A.; Atwater, H. A., Low-Loss Plasmonic Metamaterials. *Science* **2011**, *331* (6015), 290.
- 16. Shah, D.; Reddy, H.; Kinsey, N.; Shalaev, V. M.; Boltasseva, A., Optical Properties of Plasmonic Ultrathin TiN Films. *Advanced Optical Materials* **2017**, *5* (13), 1700065.
- 17. Catellani, A.; Calzolari, A., Tailoring the plasmonic properties of ultrathin TiN films at metal-dielectric interfaces. *Opt. Mater. Express* **2019**, *9* (3), 1459-1468.
- 18. Metaxa, C.; Kassavetis, S.; Pierson, J. F.; Gall, D.; Patsalas, P., Infrared Plasmonics with Conductive Ternary Nitrides. *ACS Appl. Mater. Interfaces* **2017**, *9* (12), 10825-10834.
- 19. Kassavetis, S.; Hodroj, A.; Metaxa, C.; Logothetidis, S.; Pierson, J. F.; Patsalas, P., Optical and electronic properties of conductive ternary nitrides with rare- or alkaline-earth elements. *J. Appl. Phys.* **2016**, *120* (22), 225106.
- 20. Balasubramanian, K.; Khare, S. V.; Gall, D., Valence electron concentration as an indicator for mechanical properties in rocksalt structure nitrides, carbides and carbonitrides. *Acta Mater.* **2018**, *152*, 175-185.

- 21. Wang, B.; Aryana, K.; Gaskins, J. T.; Hopkins, P. E.; Khare, S. V.; Gall, D., Structural Stabilization and Piezoelectric Enhancement in Epitaxial (Ti1–xMgx)0.25Al0.75N(0001) Layers. *Advanced Functional Materials* **2020**, *30* (23), 2001915.
- 22. Fenker, M.; Balzer, M.; Kappl, H.; Banakh, O., Some properties of (Ti,Mg)N thin films deposited by reactive dc magnetron sputtering. *Surf. Coat. Technol.* **2005**, *200* (1–4), 227-231.
- 23. Hodroj, A.; Chaix-Pluchery, O.; Steyer, P.; Pierson, J. F., Oxidation resistance of decorative (Ti,Mg)N coatings deposited by hybrid cathodic arc evaporation-magnetron sputtering process. *Surf. Coat. Technol.* **2011**, *205* (19), 4547-4553.
- 24. Mei, A. B.; Tuteja, M.; Sangiovanni, D. G.; Haasch, R. T.; Rockett, A.; Hultman, L.; Petrov, I.; Greene, J. E., Growth, nanostructure, and optical properties of epitaxial VNx/MgO(001) (0.80 [less-than-or-equal] x [less-than-or-equal] 1.00) layers deposited by reactive magnetron sputtering. *J. Mater. Chem. C* **2016**, *4* (34), 7924-7938.
- 25. Habib, A.; Florio, F.; Sundararaman, R., Hot carrier dynamics in plasmonic transition metal nitrides. *Journal of Optics* **2018**, *20* (6), 064001.
- 26. Gioti, M.; Arvanitidis, J.; Christofilos, D.; Chaudhuri, K.; Zorba, T.; Abadias, G.; Gall, D.; Shalaev, V. M.; Boltasseva, A.; Patsalas, P., Plasmonic and phononic properties of epitaxial conductive transition metal nitrides. *Journal of Optics* **2020**, *22* (8), 084001.
- 27. Tian, F.; D'Arcy-Gall, J.; Lee, T.-Y.; Sardela, M.; Gall, D.; Petrov, I.; Greene, J. E., Epitaxial Ti1-xWxN alloys grown on MgO(001) by ultrahigh vacuum reactive magnetron sputtering: Electronic properties and long-range cation ordering. *J. Vac. Sci. Technol. A* **2003**, *21* (1), 140-146.
- 28. Matenoglou, G. M.; Koutsokeras, L. E.; Patsalas, P., Plasma energy and work function of conducting transition metal nitrides for electronic applications. *Appl. Phys. Lett.* **2009**, *94* (15), 152108.
- 29. Kassavetis, S.; Abadias, G.; Vourlias, G.; Bantsis, G.; Logothetidis, S.; Patsalas, P., Optical properties of TixAl1–xN thin films in the whole compositional range. *Surface and Coatings Technology* **2016**, *295*, 125-129.
- 30. Kassavetis, S.; Bellas, D. V.; Abadias, G.; Lidorikis, E.; Patsalas, P., Plasmonic spectral tunability of conductive ternary nitrides. *Appl. Phys. Lett.* **2016**, *108* (26), 263110.
- 31. Gall, D.; Petrov, I.; Greene, J. E., Epitaxial Sc1-xTixN(001): Optical and electronic transport properties. *J. Appl. Phys.* **2001**, *89* (1), 401-409.
- 32. Gall, D.; Stoehr, M.; Greene, J., Vibrational modes in epitaxial Ti 1– x Sc x N (001) layers: An ab initio calculation and Raman spectroscopy study. *Phys. Rev. B* **2001**, *64* (17), 174302.
- 33. Greczynski, G.; Lu, J.; Johansson, M. P.; Jensen, J.; Petrov, I.; Greene, J. E.; Hultman, L., Role of Tin+ and Aln+ ion irradiation (n=1, 2) during Ti1-xAlxN alloy film growth in a hybrid HIPIMS/magnetron mode. *Surf. Coat. Technol.* **2012**, *206* (19), 4202-4211.
- 34. Deng, R.; Ozsdolay, B. D.; Zheng, P. Y.; Khare, S. V.; Gall, D., Optical and transport measurement and first-principles determination of the ScN band gap. *Phys. Rev. B* **2015**, *91* (4), 045104.
- 35. Gall, D.; Petrov, I.; Desjardins, P.; Greene, J. E., Microstructural evolution and Poisson ratio of epitaxial ScN grown on TiN(001)/MgO(001) by ultrahigh vacuum reactive magnetron sputter deposition. *J. Appl. Phys.* **1999**, 86 (10), 5524-5529.
- 36. Saha, B.; Perez-Taborda, J. A.; Bahk, J.-H.; Koh, Y. R.; Shakouri, A.; Martin-Gonzalez, M.; Sands, T. D., Temperature-dependent thermal and thermoelectric properties of n-type and p-type Sc1-xMgxN. *Phys. Rev. B* **2018**, *97* (8), 085301.
- 37. Jiang, J.; Sun, X.; Chen, X.; Wang, B.; Chen, Z.; Hu, Y.; Guo, Y.; Zhang, L.; Ma, Y.; Gao, L.; Zheng, F.; Jin, L.; Chen, M.; Ma, Z.; Zhou, Y.; Padture, N. P.; Beach, K.; Terrones, H.; Shi, Y.; Gall, D.; Lu, T.-M.; Wertz, E.; Feng, J.; Shi, J., Carrier lifetime enhancement in halide perovskite via remote epitaxy. *Nature Communications* **2019**, *10* (1), 4145.
- 38. Koh, Y. R.; Shi, J.; Wang, B.; Hu, R.; Ahmad, H.; Kerdsongpanya, S.; Milosevic, E.; Doolittle, W. A.; Gall, D.; Tian, Z.; Graham, S.; Hopkins, P. E., Thermal boundary conductance across epitaxial metal/sapphire interfaces. *Phys. Rev. B* **2020**, *102* (20), 205304.
- 39. Milosevic, E.; Kerdsongpanya, S.; McGahay, M. E.; Wang, B.; Gall, D., The Resistivity Size Effect in Epitaxial Nb(001) and Nb(011) Layers. *IEEE Trans. Electron Devices* **2019**, *66* (8), 3473-3478.

- 40. Fang, P.; Wang, B.; Mulligan, C. P.; Murray, T. M.; Khare, S. V.; Gall, D., Epitaxial growth of cubic WCy(001) on MgO(001). *J. Alloys. Compd.* **2020**, 158403.
- 41. Wang, B.; Gall, D., Fully strained epitaxial Ti1-xMgxN(001) layers. *Thin Solid Films* **2019**, *688*, 137165.
- 42. Wang, B.; Gall, D. In *A new semiconductor: Ti0.5Mg0.5N(001)*, 2018 IEEE Nanotechnology Symposium (ANTS), 14-15 Nov. 2018; IEEE: 2018; pp 1-5.
- 43. Palik, E. D., *Handbook of optical constants of solids*. Academic press: 1998; Vol. 3.
- 44. Heavens, O. S., *Optical properties of thin solid films*. Courier Corporation North Chelmsford, MA, 1991.
- 45. Wang, B.; Kerdsongpanya, S.; McGahay, M. E.; Milosevic, E.; Patsalas, P.; Gall, D., Growth and properties of epitaxial Ti1–xMgxN(001) layers. *J. Vac. Sci. Technol. A* **2018**, *36* (6), 061501.
- 46. Zhang, X. Y.; Gall, D., CrN electronic structure and vibrational modes: An optical analysis. *Phys. Rev. B* **2010**, *82* (4), 045116.
- 47. McGahay, M. E.; Wang, B.; Shi, J.; Gall, D., Band gap and electron transport in epitaxial cubic Cr1-xAlxN(001). *Phys. Rev. B* **2020**, *101* (20), 205206.
- 48. Kassavetis, S.; Ozsdolay, B. D.; Kalfagiannis, N.; Habib, A.; Tortai, J.-H.; Kerdsongpanya, S.; Sundararaman, R.; Stchakovsky, M.; Bellas, D. V.; Gall, D.; Patsalas, P., Near-Zero Negative Real Permittivity in Far Ultraviolet: Extending Plasmonics and Photonics with B1-MoNx. *J. Phys. Chem. C* **2019**.
- 49. Finnegan, N.; Haasch, R. T.; Gall, D.; Kodambaka, S.; Greene, J. E.; Petrov, I., A Comparison of Auger Electron Spectra from Stoichiometric Epitaxial TiN(001) After (1) UHV Cleaving and (2) Ar+Sputter Etching. *Surf. Sci. Spectra* **2000**, *7* (2), 93-100.
- 50. Sanjinés, R.; Wiemer, C.; Almeida, J.; Lévy, F., Valence band photoemission study of the Ti-Mo-N system. *Thin Solid Films* **1996**, *290* (Supplement C), 334-338.
- 51. Brown, E.; Odgers, K.; Giordano, M.; Lewis, K.; Berger, T.; Freedberg, J., Cylindrical films for electronics in low background physics searches. *Journal of Instrumentation* **2019**, *14* (05), P05005-P05005.
- 52. Alling, B., Metal to semiconductor transition and phase stability of Ti1-xMgxNy alloys investigated by first-principles calculations. *Phys. Rev. B* **2014**, *89* (8), 085112.
- 53. Balasubramanian, K.; Khare, S. V.; Gall, D., Energetics of point defects in rocksalt structure transition metal nitrides: Thermodynamic reasons for deviations from stoichiometry. *Acta Mater.* **2018**, *159*, 77-88.
- 54. Wang, B.; Zhang, M.; Adhikari, V.; Fang, P.; Khare, S. V.; Gall, D., Bandgap and strain engineering in epitaxial rocksalt structure (Ti0.5Mg0.5)1–xAlxN(001) semiconductors. *J. Mater. Chem. C* **2020**, *8* (36), 12677-12688.
- 55. Patsalas, P.; Logothetidis, S., Optical, electronic, and transport properties of nanocrystalline titanium nitride thin films. *J. Appl. Phys.* **2001**, *90* (9), 4725-4734.
- 56. Kang, J. H.; Kim, K. J., Structural, optical, and electronic properties of cubic TiNx compounds. *J. Appl. Phys.* **1999**, *86* (1), 346-350.
- 57. Moss, T., The interpretation of the properties of indium antimonide. *Proceedings of the Physical Society. Section B* **1954**, *67* (10), 775.
- 58. Burstein, E., Anomalous Optical Absorption Limit in InSb. Phys. Rev. 1954, 93 (3), 632-633.
- 59. Yoshihiro, I.; Mamoru, U., First-principles calculations of semiconducting TiMgN2. *Jpn. J. Appl. Phys.* **2016**, *55* (9), 098001.
- 60. Allred, A. L., Electronegativity values from thermochemical data. *J. lnorg. Nucl. Chem.* **1961,** *17* (3), 215-221.
- 61. Adachi, S.; Takahashi, M., Optical properties of TiN films deposited by direct current reactive sputtering. *J. Appl. Phys.* **2000**, 87 (3), 1264-1269.
- 62. Gall, D.; Städele, M.; Järrendahl, K.; Petrov, I.; Desjardins, P.; Haasch, R. T.; Lee, T. Y.; Greene, J. E., Electronic structure of ScN determined using optical spectroscopy, photoemission, and ab initio calculations. *Phys. Rev. B* **2001**, *63* (12), 125119.

- 63. Matenoglou, G. M.; Lekka, C. E.; Koutsokeras, L. E.; Karras, G.; Kosmidis, C.; Evangelakis, G. A.; Patsalas, P., Structure and electronic properties of conducting, ternary TixTa1-xN films. *J. Appl. Phys.* **2009**, *105* (10), 103714.
- 64. Mei, A. B.; Tuteja, M.; Sangiovanni, D. G.; Haasch, R. T.; Rockett, A.; Hultman, L.; Petrov, I.; Greene, J. E., Growth, nanostructure, and optical properties of epitaxial VNx/MgO(001) (0.80<=x<=1.00) layers deposited by reactive magnetron sputtering. *J. Mater. Chem. C* **2016**, *4* (34), 7924-7938.
- 65. Wall, M. A.; Cahill, D. G.; Petrov, I.; Gall, D.; Greene, J. E., Nucleation kinetics during homoepitaxial growth of TiN(001) by reactive magnetron sputtering. *Phys. Rev. B* **2004**, *70* (3), 035413.
- 66. Shin, C.-S.; Rudenja, S.; Gall, D.; Hellgren, N.; Lee, T.-Y.; Petrov, I.; Greene, J. E., Growth, surface morphology, and electrical resistivity of fully strained substoichiometric epitaxial TiNx  $(0.67 \le x \le 1.0)$  layers on MgO(001). *J. Appl. Phys.* **2004**, *95* (1), 356-362.
- 67. Zhang, X. Y.; Chawla, J. S.; Howe, B. M.; Gall, D., Variable-range hopping conduction in epitaxial CrN(001). *Phys. Rev. B* **2011**, *83* (16), 165205.
- 68. Shin, C.-S.; Gall, D.; Kim, Y.-W.; Desjardins, P.; Petrov, I.; Greene, J. E.; Odén, M.; Hultman, L., Epitaxial NaCl structure δ-TaNx(001): Electronic transport properties, elastic modulus, and hardness versus N/Ta ratio. *J. Appl. Phys.* **2001**, *90* (6), 2879-2885.
- 69. Seo, H.-S.; Lee, T.-Y.; Petrov, I.; Greene, J. E.; Gall, D., Epitaxial and polycrystalline HfNx (0.8≤x≤1.5) layers on MgO(001): Film growth and physical properties. *J. Appl. Phys.* **2005**, *97* (8), 083521.
- 70. West, P. R.; Ishii, S.; Naik, G. V.; Emani, N. K.; Shalaev, V. M.; Boltasseva, A., Searching for better plasmonic materials. *Laser & Photonics Reviews* **2010**, *4* (6), 795-808.

# For Table of Contents Only

Optical measurements on epitaxial rocksalt structure  $Ti_{1-x}Mg_xN$  layers with  $0.00 \le x \le 0.49$  demonstrate, in combination with transport measurements and photoelectron spectra, a tunable infrared plasmonic resonance in this refractory nitride.

